

An optimized fluorescent probe for visualizing glutamate neurotransmission

Jonathan S Marvin¹, Bart G Borghuis^{1,2}, Lin Tian^{1,7}, Joseph Cichon³, Mark T Harnett¹, Jasper Akerboom¹, Andrew Gordus⁴, Sabine L Renninger⁵, Tsai-Wen Chen¹, Cornelia I Bargmann⁴, Michael B Orger⁵, Eric R Schreiter¹, Jonathan B Demb^{2,6}, Wen-Biao Gan³, S Andrew Hires¹ & Loren L Looger¹

We describe an intensity-based glutamate-sensing fluorescent reporter (iGluSnFR) with signal-to-noise ratio and kinetics appropriate for *in vivo* imaging. We engineered iGluSnFR *in vitro* to maximize its fluorescence change, and we validated its utility for visualizing glutamate release by neurons and astrocytes in increasingly intact neurological systems. In hippocampal culture, iGluSnFR detected single field stimulus-evoked glutamate release events. In pyramidal neurons in acute brain slices, glutamate uncaging at single spines showed that iGluSnFR responds robustly and specifically to glutamate *in situ*, and responses correlate with voltage changes. In mouse retina, iGluSnFR-expressing neurons showed intact light-evoked excitatory currents, and the sensor revealed tonic glutamate signaling in response to light stimuli. In worms, glutamate signals preceded and predicted postsynaptic calcium transients. In zebrafish, iGluSnFR revealed spatial organization of direction-selective synaptic activity in the optic tectum. Finally, in mouse forelimb motor cortex, iGluSnFR expression in layer V pyramidal neurons revealed task-dependent single-spine activity during running.

Glutamate is among the most important signaling molecules in all kingdoms of life. Glutamate-gated ion channels exist in many non-animal species ranging from bacteria to plants. In the nervous system of animals, such channels (ionotropic glutamate receptors, iGluRs) form the cornerstone of information transmission at glutamatergic synapses. Extrasynaptic glutamate signaling ('spillover') activates both ionotropic and metabotropic glutamate receptors (mGluRs), located pre- and perisynaptically and also along the axonal sheath¹. In addition to its normal role in trans- and extrasynaptic transmission, glutamate is both received and released by astrocytes², the primary type of glial cell in the brain. Neuronal glutamate release mediates glial Ca²⁺ currents, directing their secretion of glutamate, ATP and D-serine, which provide feedback to regulate local neurons and vascular cells³.

Dysregulation of glutamate is implicated in receptor-mediated excitotoxicity, most notably following stroke and traumatic brain or spinal cord injury⁴ and in the progression of chronic neurodegenerative disorders such as glaucoma and Alzheimer's, Huntington's and Parkinson's diseases⁵.

Existing tools for quantitative measurement of rapid glutamate transients in intact preparations exhibit poor signal-to-noise ratio (SNR), kinetics and targetability. Historically, glutamate concentration has been determined primarily by *in situ* microdialysis⁶, but this technique is invasive and provides only single-point sampling of bulk tissue with seconds-level temporal resolution. Enzymes such as glutamate dehydrogenase or glutamate oxidase can be coupled to secondary readouts such as NADH fluorescence⁷ or current through a microelectrode⁸, but these methods lack cellular resolution, have response times on the order of a second and are confounded by other potential sources of signal.

Biosensors composed of glutamate-binding proteins coupled to a fluorescence readout address many of these concerns. Signal may be unambiguously assigned as glutamate evoked, with spatial and temporal resolutions much greater than those of diffusible secondary readouts. Modern multiphoton fluorescence microscopy allows fast, high-resolution, non-invasive imaging in awake, behaving animals⁹.

The recently developed glutamate optical sensor (EOS), a hybrid sensor made from the AMPA receptor glutamate-binding core and a small-molecule dye, produces an ~1–2% fluorescence increase in mouse somatosensory cortical neurons following limb movement^{10,11}.

Genetically encoded indicators (for a review, see ref. 12), based on autocatalytic fluorescent proteins such as GFP, may be easily targeted to specific cellular populations and subcellular compartments; they may be delivered by relatively non-invasive techniques such as viral infection or transgenesis; and they are compatible with repeated imaging over many months¹³. Genetically encoded

¹Howard Hughes Medical Institute (HHMI), Janelia Farm Research Campus, Ashburn, Virginia, USA. ²Department of Ophthalmology and Visual Science, Yale University School of Medicine, New Haven, Connecticut, USA. ³Skirball Institute of Biomolecular Medicine, New York University School of Medicine, New York, New York, USA.

⁴HHMI, Laboratory of Neural Circuits and Behavior, The Rockefeller University, New York, New York, USA. ⁵Champalimaud Neuroscience Programme, Champalimaud Centre for the Unknown, Lisbon, Portugal. ⁶Department of Cellular & Molecular Physiology, Yale University School of Medicine, New Haven, Connecticut, USA. ⁷Present address: Department of Biochemistry and Molecular Medicine, University of California Davis School of Medicine, Sacramento, California, USA. Correspondence should be addressed to L.L.L. (loogerl@janelia.hhmi.org).

RECEIVED 24 JANUARY 2012; ACCEPTED 11 DECEMBER 2012; PUBLISHED ONLINE 13 JANUARY 2013; DOI:10.1038/NMETH.2333

calcium indicators (GECIs) are the most developed, although a growing number of sensors for small molecules are available¹⁴.

Bacterial periplasmic binding proteins (PBPs) provide attractive scaffolds from which to make sensors for small-molecule metabolites. *Escherichia coli* *gltI* encodes the periplasmic component of the ABC transporter complex for glutamate and aspartate. The ligand-dependent conformational change in GltI has previously been used to create glutamate sensors, both from small-molecule dyes coupled to single introduced cysteines¹⁵, akin to EOS, and from Förster resonance energy transfer (FRET) between cyan and yellow variants of GFP fused to the two protein termini (as with FLIP-E¹⁶ and SuperGluSnFR¹⁷). FRET sensors present several advantages and drawbacks as compared to single-wavelength imaging. Ratiometry facilitates concentration determination but often lacks sensitivity owing to low changes in signal, and it simplifies motion correction but consumes greater spectral bandwidth, thus limiting multiplex imaging. Single-wavelength indicators, typically based on circularly permuted or split fluorescent proteins, are an appealing alternative to FRET sensors.

We have recently described an approach for generating high-SNR single-wavelength sensors from PBPs by the insertion of circularly permuted fluorescent proteins^{18,19}. We pioneered this technique using the *E. coli* maltose-binding protein MalE¹⁸ and extended it to the *E. coli* phosphonate-binding protein PhnD¹⁹. In both cases, high-resolution X-ray crystal structures were available in both the ligand-free, open and the ligand-bound, closed conformations. Plots of C α torsion angle differences were used to identify ligand-dependent structural changes in sequentially adjacent residues, with the expectation that such conformational changes would be well suited for modulating the fluorescence (*F*) of an inserted circularly permuted fluorescent protein. MalE and PhnD resulted in high-SNR sensors for disaccharides (($\Delta F/F$)_{max} \approx 6.5)¹⁸ and for organophosphorus compounds (($\Delta F/F$)_{max} \approx 1.6)¹⁹, respectively.

Here we report a single-wavelength glutamate sensor, iGluSnFR, constructed from *E. coli* GltI and circularly permuted (cp) GFP. iGluSnFR is bright and photostable, with 4.5 ($\Delta F/F$)_{max} *in vitro*, under both one- and two-photon illumination. In increasingly intact preparations, we show that iGluSnFR responds specifically

to glutamate *in situ*, is extremely sensitive and fast, correlates with simultaneous electrophysiology, can be used in two-color imaging and works robustly for long-term imaging in somata, dendrites and spines in retina, worms, zebrafish and mice.

RESULTS

Sensor engineering and characterization

Designing intensity-based fluorescent sensors^{18,19} requires optimization of two parameters: the cpGFP insertion site in the binding protein and the composition of the residues ('linkers') adjoining the two proteins. In previous work^{18,19}, we used quantitative structural analysis of local conformational changes that occur upon ligand binding to choose acceptable insertion positions, and we used high-throughput screening to optimize the linkers. Although no crystal structures of *E. coli* GltI are available in the protein data bank (PDB), a high-resolution structure of the 99% identical GltI from *Shigella flexneri* has been solved in the glutamate-bound state²⁰ but not in the ligand-free state. We hypothesized that the structural commonalities of our two previous sensors could be generalized to other PBPs and that on the basis of the global structural homology of *S. flexneri* GltI (PDB: 2VHA) to maltose-binding protein, we could apply these generalizations to the selection of insertion sites in GltI (Fig. 1a and Supplementary Figs. 1–7).

Placement of the cpGFP insertion point close to the interdomain hinge region (after residue 253 of GltI, Supplementary Figs. 1 and 7) followed by a screening of mutations to both linkers yielded a variant (GltI253.L1LV/L2NP) with a ($\Delta F/F$)_{max} of 4.5 ± 0.1 (s.d., *n* = 5) (Fig. 1b and Supplementary Fig. 8). Titration of purified protein *in vitro* (Fig. 1b) indicated an affinity of 107 ± 9 μ M (s.d., *n* = 5) for glutamate and 145 ± 18 μ M (*n* = 3) for aspartate (which has been identified as a co-neurotransmitter with glutamate in some neurons²¹) and a p*K*_a of 6.5 in the glutamate-bound state and 7.0 in the ligand-free state (Supplementary Fig. 9 and Online Methods). It had no detectable affinity for a panel of decoy L-amino acids (glutamine, asparagine, cysteine, arginine, histidine, serine, proline, tryptophan, β -alanine and taurine), neurotransmitters (glycine, GABA, acetylcholine, serotonin, D-serine, dopamine and its metabolic precursor L-DOPA), pharmacological glutamate receptor agonists (AMPA, NMDA, kainate)

Figure 1 | Sensor development and *in vitro* characterization. (a) Schematic of GltI–cpGFP insertion. Residues from both domains (blue and orange) contribute to the binding site for glutamate. The polypeptide chain starts in the N-terminal domain (blue), passes into the C-terminal domain (orange) and continues back through two β -strands (long pointed shapes) and into a series of helices (circles). After residue GltI253 (or other residues, identified in gray for 'failed' sensors), the polypeptide chain enters cpGFP at strand 7 (GFP residue 148), runs through cpGFP and exits (last GFP residue 147) to rejoin the remainder of GltI. The open (top), ligand-free state of the construct is dim, presumably because of distortion of the cpGFP β -barrel (tilted triangles). Binding of glutamate (star) induces a conformational change. The closed (bottom) state is bright, presumably owing to restoration of the β -barrel. (b) *In vitro* titration of L1LV/L2NP with glutamate (pink) and aspartate (orange) and *in situ* titration of iGluSnFR on HEK293 cells (green, two regions of interest (ROIs) shown) and cultured neurons (blue, three ROIs shown). (c) Two-photon fluorescence imaging of HEK293 cells expressing iGluSnFR. The green images are normalized to the peak intensity of the saturated (100 μ M glutamate) image.

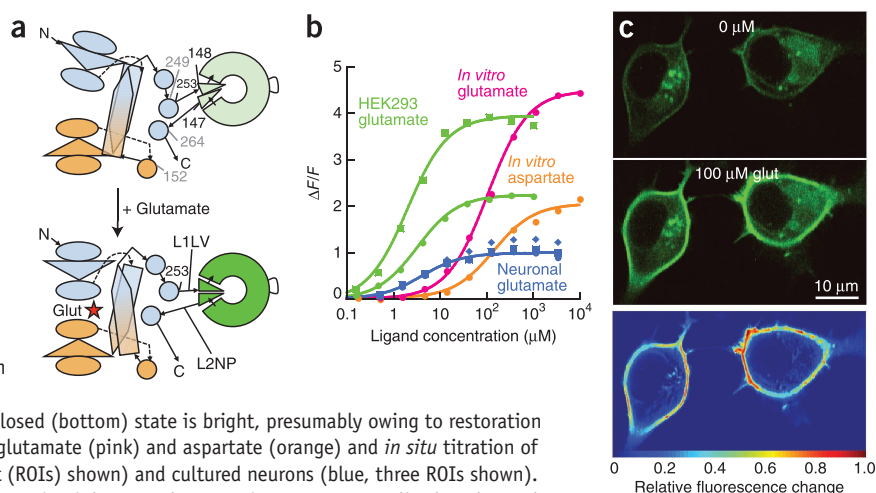
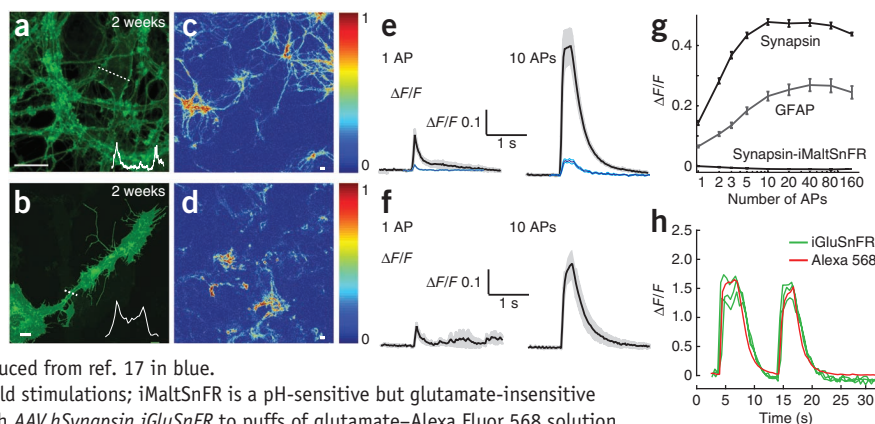


Figure 2 | Characterization of iGluSnFR in neuron-astrocyte coculture. (a,b) Expression of iGluSnFR in cultured neurons (a) and astrocytes (b) under control of synapsin and GFAP promoters, respectively. Intensity profiles in insets reflect label density in the regions shown with dotted white lines. (c,d) Fluorescent responses elicited by field stimulations in neurons (c) and astrocytes (d). Scale bars in a–d, 10 μ m. (e,f) Single field stimulus-evoked iGluSnFR responses from neurons (e; rise $t_{1/2}$ = 15 ± 11 ms, decay $t_{1/2}$ = 92 ± 11 ms, s.d., $n = 3$ for all measurements) and astrocytes (f; rise $t_{1/2}$ = 30 ± 7 ms, decay $t_{1/2}$ = 85 ± 28 ms). Relative response of SuperGluSnFR reproduced from ref. 17 in blue. (g) Amplitude of response increases with additional field stimulations; iMaltSnFR is a pH-sensitive but glutamate-insensitive control (ref. 18). (h) Response of neurons infected with AAV.hSynapsin.iGluSnFR to puffs of glutamate–Alexa Fluor 568 solution.



or antagonists (philanthotoxin PhTx-74, D-AP5, NBQX, CNQX, DNQX and CPP), or a glutamate transporter inhibitor (TBOA); nor did their presence in a glutamate titration significantly affect sensor function (Supplementary Fig. 10). The on-rate of binding was faster than could be detected by our stopped-flow fluorometer (Supplementary Fig. 11). The protein was bright and photostable under two-photon excitation (Supplementary Fig. 12), with $(\Delta F/F)_{\max}$ (≈ 4.5) similar to that under one-photon excitation (Supplementary Fig. 13). Fluorescence lifetime showed no significant glutamate-dependent change (Supplementary Fig. 13). As a preliminary test of the sensor on the surface of mammalian (human embryonic kidney HEK293) cells, the *GltI253.L1LV/L2NP* gene was cloned into the pDisplay vector (Invitrogen) for expression under control of a CMV promoter. This construct (Supplementary Fig. 14) encodes an N-terminal mouse immunoglobulin κ -chain leader sequence, which directs the protein to the secretory pathway; a hemagglutinin A (HA) epitope tag; the GltI253.L1LV/L2NP protein; a Myc epitope tag; and, at the C terminus, a platelet-derived growth factor receptor transmembrane helix, which anchors the protein to the plasma membrane, displaying it on the extracellular side. The HA tag significantly decreased $(\Delta F/F)_{\max}$ in glutamate titrations of soluble protein *in vitro* (Supplementary Fig. 15). Thus, a new version of the sensor lacking the HA tag—iGluSnFR—was cloned into the backbone of the pDisplay vector.

We measured the fluorescence of HEK293 cells transfected with *pCMV.iGluSnFR* with our two-photon microscope, using a perfusion chamber to efficiently wash cultured cells in Hank's balanced salt solution (HBSS)–glutamate solutions. The *in situ* affinity of the sensor on HEK293 cells was 4 ± 1 μ M (s.d., $n = 4$) (Fig. 1b), a 25-fold increase in affinity from that of the soluble protein and a value within the range expected to be physiologically relevant for measuring neurotransmitter release²². Although some fluorescent iGluSnFR was seen inside the cell (presumably localized to the endoplasmic reticulum), only membrane-displayed sensor responded to glutamate (Fig. 1c).

Characterization in neurons and astrocytes

To determine the suitability of iGluSnFR for detecting synaptic release of glutamate, we infected a hippocampal astrocyte–neuron coculture with adeno-associated virus (AAV2/1) under either the human synapsin-1 promoter to drive expression of iGluSnFR in neurons (AAV.hSynapsin.iGluSnFR) or the glial fibrillary acidic protein promoter to drive expression in astrocytes (AAV.GFAP.

iGluSnFR). Two weeks after infection, confocal fluorescence showed that iGluSnFR was evenly distributed on the extracellular surface of neuronal somata and dendrites (Fig. 2a). Expression of iGluSnFR on the extracellular surface remained fairly stable after 4 weeks (Supplementary Fig. 16). Titration with glutamate in a flow cell indicated an *in situ* affinity of the sensor on the neuron surface of 4.9 ± 1.3 μ M (s.d., $n = 3$ ROIs) (Fig. 1b), with $(\Delta F/F)_{\max} = 1.03 \pm 0.15$. In astrocytes, the fluorescence of iGluSnFR was uniformly distributed on the membrane of somata and processes, but with some puncta apparent (Fig. 2b).

To test the performance of iGluSnFR in resolving action potential (AP)-evoked glutamate transients, we delivered a series of electrical field stimuli at 30 Hz (one field stimulus evokes one AP, data not shown). iGluSnFR was sensitive enough to detect global glutamate release from single field stimuli, in both somata and processes of neurons (Fig. 2c), and on astrocytes cocultured with neurons (Fig. 2d). In neurons, increases in iGluSnFR fluorescence were detected in response to single APs (Fig. 2e, field of view $(\Delta F/F)_{\max} = 0.14 \pm 0.02$; s.d., $n = 3$ trials); on astrocytes, single AP-induced glutamate release from neurons was reliably detected, but with a lower magnitude change in fluorescence (Fig. 2f, $(\Delta F/F)_{\max} = 0.07 \pm 0.01$). For both cell types, the peak fluorescence plateaued at higher numbers of AP stimuli (20–160 APs) (Fig. 2g), with additional stimulations increasing the duration of the fluorescent signal but not the amplitude. iGluSnFR also showed fast kinetics on both cells (Fig. 2e,f); decay time increased with more AP stimuli (Supplementary Fig. 17). SNR in neurons was significantly larger than in previously reported data measured with SuperGluSnFR¹⁷ under similar conditions (Fig. 2e).

To confirm that the observed change in fluorescence was the result of glutamate release and not an artifact caused, for example, by a change in pH at the synapse, AAV.hSynapsin.iMaltSnFR¹⁸, which has a pH profile similar to that of iGluSnFR (Supplementary Figs. 9 and 18), was tested as well and showed no response (Fig. 2g).

Finally, cultured hippocampal neurons were imaged in a perfusion chamber with two-photon illumination and subjected to 'puffs' of glutamate. After an extensive wash with HBSS to restore the sensor to a glutamate-free state (neuronal culture growth medium contains 5% FBS and ~ 100 μ M glutamate, Supplementary Fig. 19), a patch pipette filled with 37 μ M glutamate and 1 nM Alexa Fluor 568 (as a red tracer) was

Figure 3 | Two-photon glutamate uncaging-evoked iGluSnFR signals in acute hippocampal slices. **(a,b)** Two-photon images of apical oblique **(a)** and basal **(b)** dendritic branch segments from CA1 hippocampal neurons filled via somatic patch pipettes with Alexa Fluor 594. Yellow and blue symbols indicate locations of line scans through spine heads for iGluSnFR imaging at 920 nm (lines) and focal uncaging of MNI-glutamate at 720 nm (circles). Voltage traces recorded at somata (top traces) and local spine head iGluSnFR signals (bottom traces) are shown for single-pulse (0.2-ms dwell time) uncaging at three different laser powers (all traces are means of 3–6 trials). Voltage, time and fluorescence scale values as in **a** **(c,d)** Summary of iGluSnFR signals **(c)**, $(\Delta F/F)_{\text{peak}}$; **d**, area) as a function of somatic excitatory postsynaptic potential amplitude evoked by single pulse two-photon uncaging (GluEPSP) for 28 apical oblique and basal dendritic spines. Points connected by lines represent uncaging at increasing power at individual spines; colors match traces from **a** and **b**. **(e)** EPSP and iGluSnFR signals (top and bottom traces, respectively) in the presence (brown) or absence (gray) of MNI-glutamate. **(f)** EPSP and iGluSnFR signals when uncaging (circles) and imaging (lines) are performed distal to (light orange) or near (dark orange) the relevant dendrite. **(g)** EPSP and iGluSnFR signals at three spines when glutamate is uncaged at only the center spine (green). Scale bars for all two-photon images, 1 μm . Voltage, time and fluorescence scale values for **f,g** as in **e**.

brought near the neurons. We puffed a small amount of the mixture onto the neurons during continuous perfusion of glutamate-free HBSS by briefly applying positive pressure to the patch pipette (<200 ms). Green fluorescence was observed to increase rapidly and coincidentally with red fluorescence and decay just slightly slower than diffusion of the red signal. Repeated puffs evoked similar fluorescence responses (**Fig. 2h**).

Two-photon glutamate uncaging and imaging in brain slices

To characterize the sensitivity and kinetics of iGluSnFR in the context of its applicability for studying mammalian synaptic transmission, we used two-photon glutamate uncaging and imaging in acute rat hippocampal slices²³. Two to four weeks after viral delivery of *AAV.hSynapsin.iGluSnFR* into the hippocampus, infected pyramidal neurons in CA1, CA2 and subiculum were patched and filled with Alexa Fluor 594. This anatomical dye enabled glutamate uncaging to be targeted at spine heads located on perisomatic apical oblique and basal dendrites within ~120 μm of the soma. Line scans were recorded at 600–1,200 Hz (excited with a second laser at 920 nm) on the spine heads where glutamate was uncaged (**Fig. 3**). The whole-cell patch electrode recorded cellular electrical responses in current-clamp mode.

Resting membrane potential of iGluSnFR-expressing pyramidal neurons appeared normal (-65.0 ± 0.5 mV, s.e.m., $n = 9$ neurons). Large, fast iGluSnFR signals were observed at all spines tested (**Fig. 3a,b**, $n = 28$ spines from nine neurons taken from five animals), including at uncaging laser intensities that evoked physiologically sized excitatory postsynaptic potentials (EPSPs) at the soma²³. Peak amplitude (**Fig. 3c**) and time-integrated area (**Fig. 3d**) of iGluSnFR signals correlated roughly linearly with somatic EPSP amplitude. Single-trial results are shown in **Supplementary Figure 20**. Responses to single uncaging pulses were extremely rapid (~5 ms). Notably, at some spines iGluSnFR responded to very low uncaging laser intensities that produced no EPSP signals above background (**Fig. 3b**). We confirmed the necessity of MNI-glutamate by showing that iGluSnFR and EPSP signals decreased substantially when MNI-glutamate application was discontinued

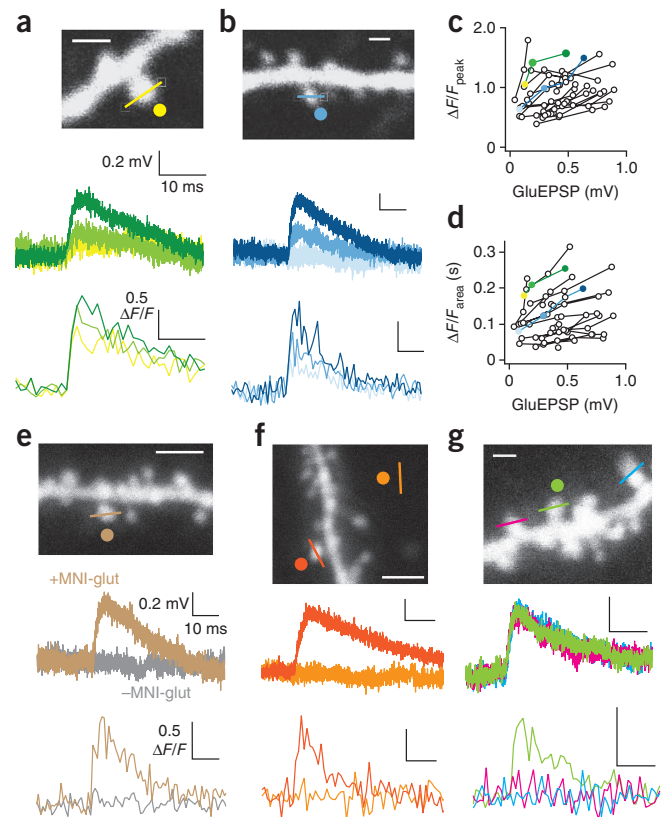


(**Fig. 3e**, $n = 2$). The contribution of background glutamate was negligible, as shown by the absence of iGluSnFR and EPSP signals when uncaging and imaging were performed remotely from the relevant dendrite (**Fig. 3f**, $n = 3$). Glutamate uncaged at one spine produced no measurable response in spines >2 μm away (**Fig. 3g**, $n = 4$ spines from two neurons). These experimental results indicate that iGluSnFR sensitively and rapidly reports glutamate dynamics at relevant cellular structures within the physiological regime for neurotransmission in intact brain tissue.

Mouse retina *in vitro* imaging

Glutamate is the predominant excitatory neurotransmitter in the mammalian retina²⁴. In the inner plexiform layer (IPL), ON-type bipolar cells release glutamate onto ON-type ganglion cells following light increments, whereas OFF-type bipolar cells release glutamate onto OFF-type ganglion cells following light decrements. The ON and OFF bipolar cell axon terminals stratify in separate halves of the IPL: ON bipolar terminals stratify in the proximal half, whereas OFF bipolar terminals stratify in the distal half²⁴. The known functional anatomy of glutamate release in the retina was used to test iGluSnFR responses to synaptic activity in an intact neural circuit.

iGluSnFR was expressed in ganglion cells of adult mice (>4 weeks) by viral transduction of *AAV.hSynapsin.iGluSnFR*. Retinas showed robust iGluSnFR expression in the IPL 14 d post-injection (**Supplementary Fig. 21**). At 14–21 d post-injection, we targeted for whole-cell recording an iGluSnFR-expressing ganglion cell of the OFF-delta type (OFF sustained²⁵) (**Fig. 4a**). The voltage-clamped cell showed robust excitatory postsynaptic currents in response to light stimulation (**Fig. 4b**), confirming

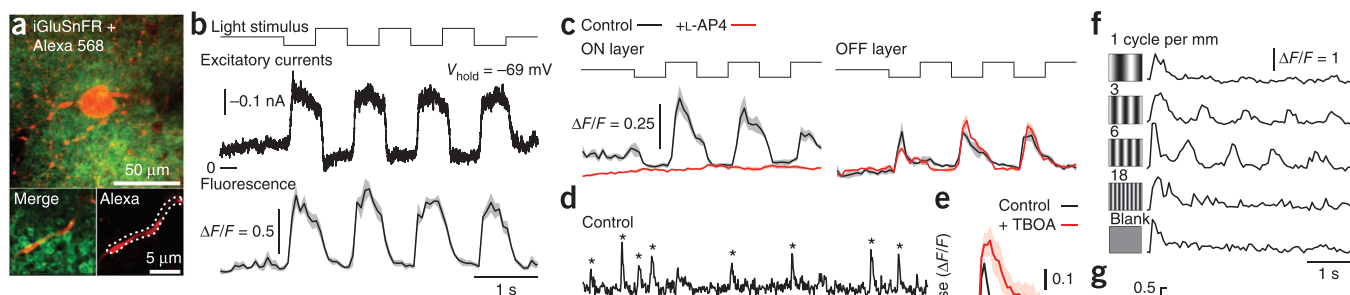


Figure 4 | Imaging glutamate in mouse retina *in vitro*.

(a) Two-photon fluorescence images of iGluSnFR-expressing dendrites (green) in the inner plexiform layer (IPL). Top, z projection of an iGluSnFR-expressing ganglion cell that was selected for whole-cell recording and filled with a red fluorescent dye (Alexa Fluor 568). Bottom, single image planes that include the region of interest (ROI) used for analysis of light-evoked fluorescence responses (dashed white line). (b) Simultaneous patch-clamp and fluorescence recordings (frame scan, 16 frames per second) from the cell shown in a (average of 8 repetitions, \pm s.e.m. for fluorescence, shown in gray). Excitatory currents have been inverted for comparison (negative current goes upward). Light stimulus was a 150- μ m diameter spot, modulated at 100% Michelson contrast (peak wavelength, 398 nm). (c) iGluSnFR responses with or without L-AP4 (20 μ M) in the ON and OFF layers of the IPL (\pm s.e.m., $n = 4$). (d) Spontaneous fluorescence responses (asterisks) recorded with line scans (500 lines per second; ROI contained the cross-section of a single iGluSnFR-expressing dendrite) in the OFF layer of the IPL during constant background illumination in the absence (top) or presence of TBOA (40 μ M, bottom). (e) Shape of the average spontaneous fluorescence event in the absence or presence of TBOA (mean \pm s.e.m., $n = 19$ and 15 events, respectively). (f) Fluorescence responses to drifting spatial sine wave stimuli recorded in the ON layer of the IPL (traces show single trials; 90% Michelson contrast). (g) Amplitude of a sine wave fit to the data shown in f (mean \pm s.e.m. of six repetitions).

that iGluSnFR did not interfere with excitatory synaptic transmission. Fluorescence responses simultaneously recorded from the dendritic arbor in the OFF stratum of the IPL (Fig. 4a) correlated with excitatory postsynaptic currents during the dark phase of the stimulus (Fig. 4b), consistent with glutamate release from OFF bipolar cells.

To confirm that light-evoked fluorescence changes signaled glutamate release, we tested the effect of selectively blocking ON bipolar cells. ON bipolar cells express the sign-inverting mGluR6 receptor at their dendrites, whereas OFF bipolar cells instead express iGluRs²⁴. An agonist of mGluR6 receptors, L-AP4, selectively hyperpolarizes ON bipolar cells, blocking their synaptic release, but it does not block release from OFF bipolar cells²⁴. L-AP4 selectively blocked iGluSnFR signals in the ON stratum but not the OFF stratum of the IPL, confirming that the iGluSnFR signal was dependent on glutamate release from bipolar cells (Fig. 4c).

In the presence of steady background light, neurites in the OFF stratum of the IPL showed sparse, spontaneous fluorescence events. The glutamate reuptake inhibitor DL-threo- β -benzyloxyaspartate (TBOA, 40 μ M), which blocks EAAT1 and EAAT2 (ref. 26), increased both the amplitude and the decay time constant of these spontaneous fluorescence events (Fig. 4d,e). The increased response in TBOA is consistent with a reduced rate of glutamate removal from the synaptic cleft.

We tested whether iGluSnFR could be used to measure receptive fields of bipolar cells at the level of their synaptic outputs. In response to drifting sine-wave gratings of increasing spatial frequency (Fig. 4f), modulation of the iGluSnFR fluorescence peaked at about six cycles per millimeter. This tuning is consistent with surround inhibition at low spatial frequencies. At high frequencies (more than ten cycles per millimeter), bright and dark stimulus regions covered the receptive field simultaneously and response modulation was reduced (Fig. 4f,g). These

measurements are consistent with the known receptive field size of bipolar cells^{27,28}.

In vivo glutamate and calcium signaling in *C. elegans*

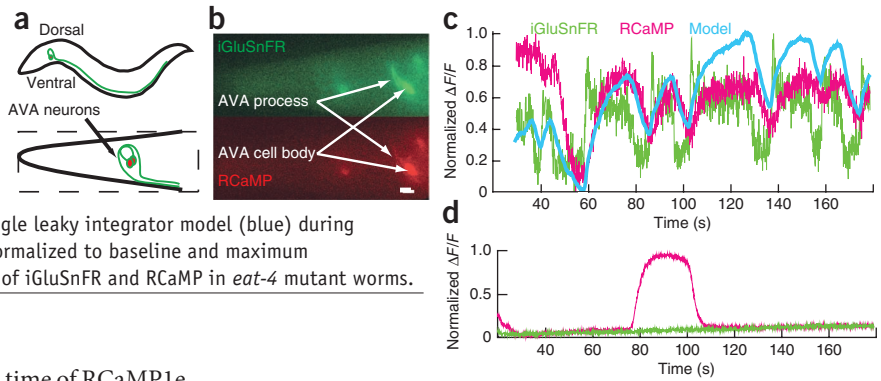
To demonstrate the *in vivo* functionality of iGluSnFR, it was tested in three animal species: worm, zebrafish and mouse. The nematode *Caenorhabditis elegans* has 302 neurons, many of which are glutamatergic. The left and right AVA neurons are command interneurons located in the head lateral ganglia that play an essential role in the reverse locomotion circuit²⁹. Each AVA neuron is postsynaptic to 40 other neurons³⁰. In the nerve ring, the AVA neurons make only postsynaptic connections; nerve ring iGluSnFR signal from these neurons should thus be exclusively postsynaptic. The AVA neurons express NMDA- and AMPA-type iGluRs as well as a glutamate-gated chloride channel³¹, but they appear not to express EAT-4, the primary vesicular glutamate transporter³². The role of AVA as integrators of presynaptic signals and their lack of glutamatergic vesicles make these useful neurons in which to test the ability of iGluSnFR to report postsynaptic glutamate.

We monitored glutamate input into AVA and AVA somatic calcium simultaneously using iGluSnFR and the recently developed red genetically encoded calcium indicator RCaMP³³, both under the control of the *rig-3* promoter. iGluSnFR expression was strongest along the neuronal process in the nerve ring, and RCaMP1e expression was strongest at the soma (Fig. 5a,b). Fluorescence from the neuronal process in the nerve ring was used to detect glutamate input (from iGluSnFR), and fluorescence from the cell body was used to detect calcium output (from RCaMP). We observed that iGluSnFR responses reliably preceded RCaMP responses (Fig. 5c), consistent with existing evidence that glutamate provides strong excitation to AVA, leading to reversal behavior²⁹.

A delay of a few seconds in the cell body RCaMP1e response likely reflects the indirect relationship between depolarization and

Figure 5 | Glutamatergic input into *C. elegans* AVA neurons and resulting somatic $[Ca^{2+}]$ signal.

(a) Cartoon of *C. elegans* and AVA neurons (left and right). (b) Fluorescence micrographs of iGluSnFR and RCaMP1e simultaneously expressed in AVA; the region imaged is denoted by the dashed box in a. Scale bar, 10 μ m. (c) Overlay of iGluSnFR fluorescence changes (green), somatic RCaMP fluorescence changes (pink) and a single leaky integrator model (blue) during spontaneous AVA activity. Fluorescence signals are normalized to baseline and maximum fluorescence in each trace. (d) Fluorescence changes of iGluSnFR and RCaMP in *eat-4* mutant worms.



calcium as well as the low affinity and slow rise time of RCaMP1e, which produces a strong fluorescence response only above $\sim 1\text{--}2\text{ }\mu\text{M}$ $[Ca^{2+}]$ (data not shown). A simple integrator-type computational model shows a direct correlation between the presumed glutamatergic input measured with iGluSnFR and the resulting calcium signal inferred by somatic RCaMP (Fig. 5c). A single leaky integrator yields a good fit to the experimental data in amplitude and relative timing (Supplementary Figs. 22 and 23). This relationship supports a circuit model in which glutamatergic input correlates with both the timing and the magnitude of subsequent AVA output and is consistent with existing circuit diagram models of AVA neurons and the surrounding nerve ring.

To demonstrate that the signal detected by iGluSnFR was specifically related to glutamate release, we examined *eat-4(ky5)* mutants, which are defective in the vesicular glutamate transporter that loads glutamate into synaptic vesicles. AVA calcium transients in *eat-4* mutants were not accompanied by increased fluorescence of iGluSnFR (Fig. 5d and Supplementary Fig. 24), suggesting that iGluSnFR specifically detects a glutamate-associated signal and not general AVA activity. It should be noted that *eat-4* mutants exhibited a reduced number but normal amplitude of RCaMP calcium transients in AVA neurons, consistent with previous results demonstrating that excitatory glutamatergic transmission is one of several inputs that can activate AVA and backward movement³².

In vivo imaging in fish and mice

In larval zebrafish, iGluSnFR reliably reported spatial organization of direction-selective synaptic activity in the optic tectum, consistent with but more rapid than GECIs³⁴ (Supplementary Figs. 25–27).

To evaluate iGluSnFR functionality in the intact rodent brain, we delivered iGluSnFR to layer V of the motor cortex via infection of AAV.*hSynapsin.iGluSnFR* in juvenile mice (postnatal day P20–P30) (Fig. 6a). Two weeks after infection, two-photon imaging *in vivo* revealed densely packed yet resolvable individual dendrites, which were clearly visible in the superficial layers (Fig. 6b). In post-fixed brain slices, confocal imaging in layer V revealed sparse labeling of cells, and individual somata displayed a halo-like expression pattern with iGluSnFR clearly perimembrane (Supplementary Fig. 28). Neuropil was also strongly labeled.

After iGluSnFR expression, head-fixing posts were implanted and mice were imaged while in a resting-awake state or while they were running on a free-floating treadmill (Fig. 6c). Because individual dendrites are clearly resolvable under low-density labeling conditions, we tested whether glutamate transients

could be detected in the apical tuft dendrites of layer V neurons of awake, behaving animals by two-photon microscopy in primary motor cortex (M1), in the region specific to forelimb representation (spatial coordinates taken from ref. 35). In mice that were anesthetized (with a mixture of ketamine and xylazine), we frequently observed spontaneous, repetitive glutamate transients over hours (Supplementary Fig. 29), consistent with the observation by microdialysis that ketamine increases extracellular glutamate³⁶. In resting-awake animals, we observed numerous transient glutamate events with large $(\Delta F/F)_{\text{max}}$ ($\sim 0.2\text{--}0.4$, Fig. 6c and Supplementary Fig. 30). Additionally, we detected glutamate transients in single dendritic spines over time during head-fixed running (Fig. 6c).

We next imaged iGluSnFR fluorescence in response to motor tasks. Head-fixed animals were subjected to forward or reverse (backward) running on a free-floating treadmill. Fast scanning of small cortical regions of interest (ROIs) revealed robust and reliable glutamate responses during running (Fig. 6c,d). Peak iGluSnFR responses were restricted to small regions, whose size ($\sim 0.25\text{ }\mu\text{m} \times 0.25\text{ }\mu\text{m}$), shape and proximity to the dendritic shaft are indicative of spine heads. Moreover, iGluSnFR revealed dendritic segments containing multiple spines sensing many glutamate events during trials of forward running (Supplementary Fig. 31). Spines reporting glutamate events on these dendritic segments were clustered on the same branch, but their responses were uncoordinated. Consistent with the fast timescale of neurotransmission, line scanning of a spine head and its associated dendritic shaft during running showed fast kinetics of a glutamate transient (on only the spine head) that lasted $\sim 50\text{--}100$ ms (Fig. 6d,e).

Glutamate events were associated with either running or running direction (that is, reverse only or forward only; Fig. 6f), with large changes in fluorescence (up to $0.55 (\Delta F/F)_{\text{max}}$). No glutamate transients were detected under awake-resting conditions or forward running in ROIs 1 and 2. A different ROI (3) within the field of view activated under only forward running conditions. Events typically commenced upon running onset and stopped upon running cessation (Fig. 6g). These glutamate events were highly reproducible across several running trials. Furthermore, we found that local application of tetrodotoxin via a small craniotomy (Supplementary Fig. 32) effectively blocked running-related glutamate transients along apical tuft dendrites (Fig. 6h). Intraperitoneal injection of pilocarpine (a nonselective muscarinic receptor agonist) produced seizures in the mice and doubled the amplitude of observed glutamate events (Supplementary Fig. 33). Thus, iGluSnFR provides a reliable means for investigating

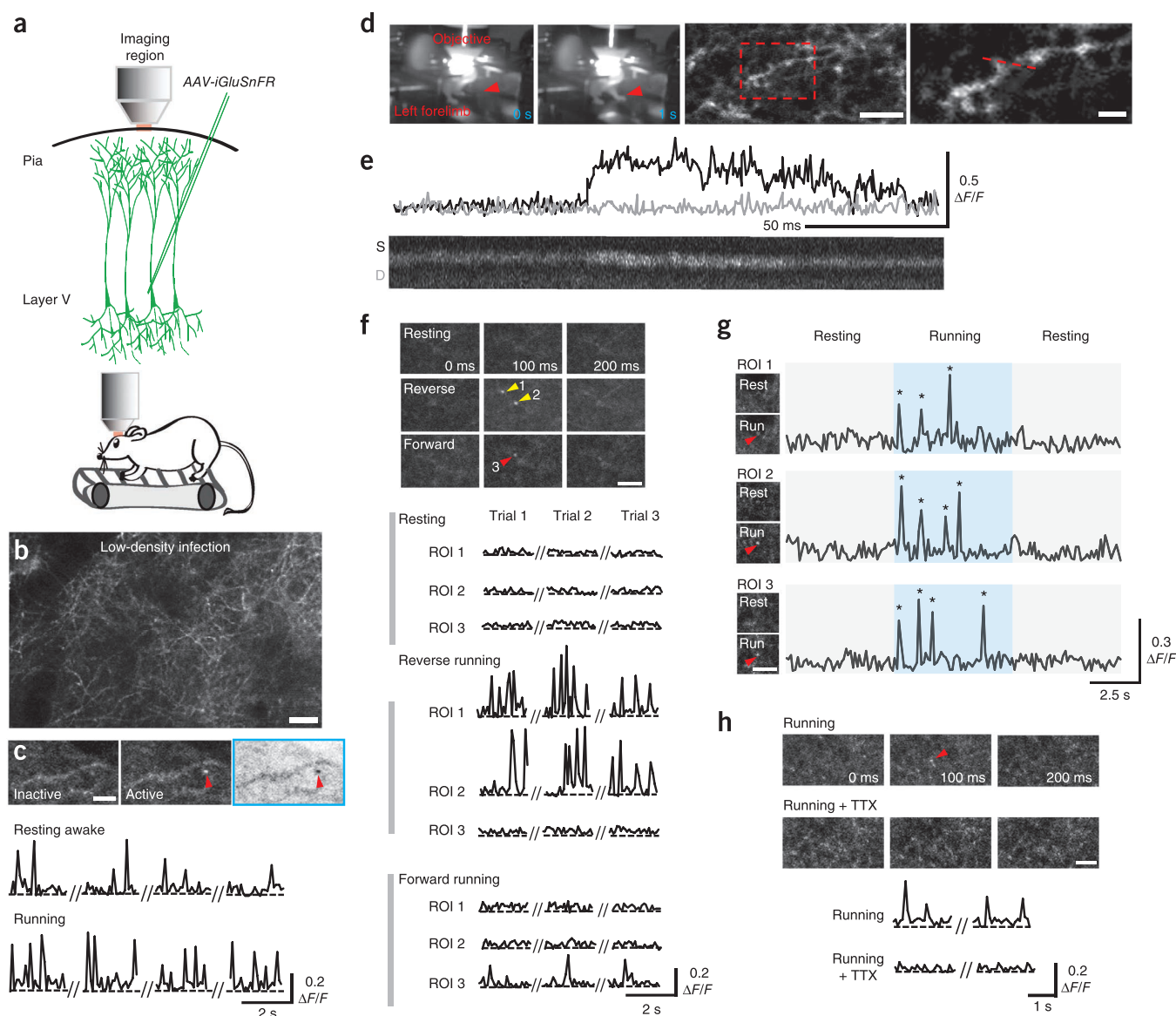


Figure 6 | *In vivo* imaging of awake behavior and motor task-associated glutamate transients in mouse primary motor cortex. **(a)** Schematic illustrating experimental approach for injection of AAV-*iGluSnFR* into layer V of primary motor cortex for *in vivo* transcranial two-photon microscopy. **(b)** Two-photon image of low-density infection of primary motor cortex (forelimb region) with AAV-*iGluSnFR*. Scale bar, 10 μm . **(c)** Low-density viral labeling of *iGluSnFR* showing apparent dendritic spines (arrowheads) that show repetitive glutamate transients (four 2-s traces shown) during awake resting (top; seven events over 8 s) and forward running (bottom; 15 events detected during running over 8 s). Average $\Delta F/F$ during running was $27\% \pm 1.9\%$ s.e.m. versus $23\% \pm 3.2\%$ while resting. Scale bar, 2 μm . **(d)** Line scan of a dendritic segment in an awake animal running on the treadmill. Two leftmost subpanels, photographs of a head-fixed animal undergoing left forelimb movement (arrowheads). Two rightmost subpanels, two-photon images of a dendritic segment from the apical tuft of motor cortex. Scale bars, 2 μm (third subpanel) and 5 μm (fourth subpanel). Boxed region contains the dendritic spine of interest. **(e)** Spine and associated dendrite fluorescent response traces of line scan depicted in **d**. S (black), spine; D (gray), associated dendrite. **(f)** *iGluSnFR* detection of task-specific glutamate responses during motor training. Example traces are shown of fluorescence changes (2-s recordings) during three trials of reverse and forward running as well as awake-resting state. Arrowheads indicate glutamate events for reverse running only (yellow) or forward running only (red). ROI, region of interest. **(g)** *iGluSnFR* signals during periods of locomotion. Asterisks, glutamate events. ROIs are distinct from those in **f**. **(h)** Effect of tetrodotoxin (TTX, 1 nM in artificial cerebrospinal fluid), delivered via a small craniotomy lateral to the thinned-skull imaging region (Supplementary Fig. 32), on running-related glutamate transients (red arrowhead marks a glutamate transient during running) along apical tuft dendrites. Scale bar, 10 μm .

glutamate transients in single dendritic spines as well as dendritic branches in awake behaving mice.

DISCUSSION

Not only is glutamate an important chemical messenger in neurobiology, it has many other signaling roles, is central to amino

acid metabolism in plants³⁷ and is a major industrial fermentation product³⁸. Tools for detecting glutamate are thus of broad utility. Classical methods for monitoring glutamate, such as microdialysis, are limited by poor spatial and temporal resolution. Recently developed fluorescent sensors, such as FLIP-E¹⁶, SuperGluSnFR¹⁷ and EOS^{10,11}, have low signal change and have

yet to be used beyond initial proof-of-principle experiments. Recent cell-based sensors of neurotransmitters (CNiFERS)³⁹ access just the bulk medium and are slow, allowing only volume transmission to be visualized. In contrast, iGluSnFR rapidly and directly accesses the synaptic cleft, with large SNR *in vivo*.

In addition to having advantages over existing glutamate sensors, iGluSnFR may be better suited than calcium indicators for reporting neuronal input and activity in some situations. Detection of [Ca²⁺] transients in axon terminals is a common proxy for estimating synaptic release. However, the coupling between presynaptic [Ca²⁺] and transmitter release collapses when vesicle pools are depleted following sustained stimulation⁴⁰, and it is modified in interesting and more subtle ways by activity-dependent synaptic depression and facilitation. iGluSnFR directly and specifically reports excitatory synaptic release. Postsynaptic iGluSnFR expression should allow determination of the timing and localization of excitatory synaptic input from distinct classes of afferent neurons across a dendritic arbor. Indicator variants with altered affinity may be required for investigating the full complement of glutamatergic synapse types⁴¹. (The ~4 μ M affinity of iGluSnFR precludes quantitation of the millimolar glutamate concentrations estimated following heavy release²².) Coexpression with a second fluorescent protein should aid in reconstructing morphology of iGluSnFR 'hot spots'. With improved imaging and analysis methods, we anticipate that iGluSnFR will be embraced as a useful complement to calcium imaging to deconvolve neural activity into its composite molecular signaling events.

METHODS

Methods and any associated references are available in the [online version of the paper](#).

Accession codes. Addgene: pCMV.iGluSnFR (41732) and pRSET.GltI253-cpGFP.L1LV/L2NP (41733). AAV virus also available; see Online Methods.

Note: Supplementary information is available in the [online version of the paper](#).

ACKNOWLEDGMENTS

We thank J. Macklin for two-photon spectrophotometry and two-photon lifetime measurements of purified proteins; H. White and S. Winfried for tissue culture; B. Shields and A. Hu for mouse brain dissection and neuronal culture; Molecular Biology and Media Prep Shared Resources for DNA preparation and sequencing and for media preparation; M. Ramirez and K. Ritola for virus production; D. Kim and the GECI Project for advice and use of the neuronal culture rig; and K. Svoboda, J. Magee and A. Hantman for helpful conversations. All affiliations are HHMI Janelia Farm. HHMI supported this work.

AUTHOR CONTRIBUTIONS

J.S.M. and L.L.L. conceived of the project. J.S.M. designed iGluSnFR and performed *in vitro* and cultured cell characterization; L.T. characterized cultured neurons and astrocytes; M.T.H. performed glutamate uncaging experiments; B.G.B. and J.B.D. characterized retina; A.G. and C.I.B. characterized worms; S.L.R. and M.B.O. characterized zebrafish; J.C. and W.-B.G. characterized mouse motor cortex; J.A. and E.R.S. provided RCaMP1e; T.-W.C. assisted with data analysis; S.A.H. and L.L.L. provided global perspective and planning of experiments across species.

COMPETING FINANCIAL INTERESTS

The authors declare competing financial interests: details are available in the [online version of the paper](#).

Published online at <http://www.nature.com/doi/10.1038/nmeth.2333>. Reprints and permissions information is available online at <http://www.nature.com/reprints/index.html>.

- Kullmann, D.M. & Asztely, F. Extrasynaptic glutamate spillover in the hippocampus: evidence and implications. *Trends Neurosci.* **21**, 8–14 (1998).
- Haydon, P.G. GLIA: listening and talking to the synapse. *Nat. Rev. Neurosci.* **2**, 185–193 (2001).
- Nedergaard, M., Ransom, B. & Goldman, S.A. New roles for astrocytes: redefining the functional architecture of the brain. *Trends Neurosci.* **26**, 523–530 (2003).
- Choi, D.W. Excitotoxic cell death. *J. Neurobiol.* **23**, 1261–1276 (1992).
- Parsons, C.G., Danyisz, W. & Quack, G. Glutamate in CNS disorders as a target for drug development: an update. *Drug News Perspect.* **11**, 523–569 (1998).
- Benveniste, H., Drejer, J., Schousboe, A. & Diemer, N.H. Elevation of the extracellular concentrations of glutamate and aspartate in rat hippocampus during transient cerebral ischemia monitored by intracerebral microdialysis. *J. Neurochem.* **43**, 1369–1374 (1984).
- Innocenti, B., Parpura, V. & Haydon, P.G. Imaging extracellular waves of glutamate during calcium signaling in cultured astrocytes. *J. Neurosci.* **20**, 1800–1808 (2000).
- Hu, Y., Mitchell, K.M., Albadily, F.N., Michaelis, E.K. & Wilson, G.S. Direct measurement of glutamate release in the brain using a dual enzyme-based electrochemical sensor. *Brain Res.* **659**, 117–125 (1994).
- Kerr, J.N. & Denk, W. Imaging *in vivo*: watching the brain in action. *Nat. Rev. Neurosci.* **9**, 195–205 (2008).
- Namiki, S., Sakamoto, H., Iinuma, S., Iino, M. & Hirose, K. Optical glutamate sensor for spatiotemporal analysis of synaptic transmission. *Eur. J. Neurosci.* **25**, 2249–2259 (2007).
- Okubo, Y. *et al.* Imaging extrasynaptic glutamate dynamics in the brain. *Proc. Natl. Acad. Sci. USA* **107**, 6526–6531 (2010).
- Okumoto, S. Imaging approach for monitoring cellular metabolites and ions using genetically encoded biosensors. *Curr. Opin. Biotechnol.* **21**, 45–54 (2010).
- Tian, L. *et al.* Imaging neural activity in worms, flies and mice with improved GCaMP calcium indicators. *Nat. Methods* **6**, 875–881 (2009).
- Frommer, W.B., Davidson, M.W. & Campbell, R.E. Genetically encoded biosensors based on engineered fluorescent proteins. *Chem. Soc. Rev.* **38**, 2833–2841 (2009).
- de Lorimier, R.M. *et al.* Construction of a fluorescent biosensor family. *Protein Sci.* **11**, 2655–2675 (2002).
- Okumoto, S. *et al.* Detection of glutamate release from neurons by genetically encoded surface-displayed FRET nanosensors. *Proc. Natl. Acad. Sci. USA* **102**, 8740–8745 (2005).
- Hires, S.A., Zhu, Y. & Tsien, R.Y. Optical measurement of synaptic glutamate spillover and reuptake by linker optimized glutamate-sensitive fluorescent reporters. *Proc. Natl. Acad. Sci. USA* **105**, 4411–4416 (2008).
- Marvin, J.S., Schreiter, E.R., Echevarri, I.M. & Looger, L.L. A genetically encoded, high-signal-to-noise maltose sensor. *Proteins* **79**, 3025–3036 (2011).
- Alicea, I. *et al.* Structure of the *Escherichia coli* phosphonate binding protein PhnD and rationally optimized phosphonate biosensors. *J. Mol. Biol.* **414**, 356–369 (2011).
- Hu, Y. *et al.* Crystal structure of a glutamate/aspartate binding protein complexed with a glutamate molecule: structural basis of ligand specificity at atomic resolution. *J. Mol. Biol.* **382**, 99–111 (2008).
- Nadler, J.V. Aspartate release and signalling in the hippocampus. *Neurochem. Res.* **36**, 668–676 (2011).
- Clements, J.D. Transmitter timecourse in the synaptic cleft: its role in central synaptic function. *Trends Neurosci.* **19**, 163–171 (1996).
- Losonczy, A. & Magee, J.C. Integrative properties of radial oblique dendrites in hippocampal CA1 pyramidal neurons. *Neuron* **50**, 291–307 (2006).
- Miller, R.F. Cell communication mechanisms in the vertebrate retina the proctor lecture. *Invest. Ophthalmol. Vis. Sci.* **49**, 5184–5198 (2008).
- Margolis, D.J. & Detwiler, P.B. Different mechanisms generate maintained activity in ON and OFF retinal ganglion cells. *J. Neurosci.* **27**, 5994–6005 (2007).
- Shimamoto, K. *et al.* dl-threo- β -benzyloxyaspartate, a potent blocker of excitatory amino acid transporters. *Mol. Pharmacol.* **53**, 195–201 (1998).
- Berntson, A. & Taylor, W.R. Response characteristics and receptive field widths of on-bipolar cells in the mouse retina. *J. Physiol. (Lond.)* **524**, 879–889 (2000).
- Schwartz, G.W. *et al.* The spatial structure of a nonlinear receptive field. *Nat. Neurosci.* **15**, 1572–1580 (2012).
- Chalfie, M. *et al.* The neural circuit for touch sensitivity in *Caenorhabditis elegans*. *J. Neurosci.* **5**, 956–964 (1985).

30. White, J.G., Southgate, E., Thomson, J.N. & Brenner, S. The structure of the nervous system of the nematode *Caenorhabditis elegans*. *Phil. Trans. R. Soc. Lond. B* **314**, 1–340 (1986).
31. Mellem, J.E., Brockie, P.J., Zheng, Y., Madsen, D.M. & Maricq, A.V. Decoding of polymodal sensory stimuli by postsynaptic glutamate receptors in *C. elegans*. *Neuron* **36**, 933–944 (2002).
32. Brockie, P.J., Madsen, D.M., Zheng, Y., Mellem, J. & Maricq, A.V. Differential expression of glutamate receptor subunits in the nervous system of *Caenorhabditis elegans* and their regulation by the homeodomain protein UNC-42. *J. Neurosci.* **21**, 1510–1522 (2001).
33. Husson, S.J. *et al.* Optogenetic analysis of a nociceptor neuron and network reveals ion channels acting downstream of primary sensors. *Curr. Biol.* **22**, 743–752 (2012).
34. Akerboom, J. *et al.* Optimization of a GCaMP calcium indicator for neural activity imaging. *J. Neurosci.* **32**, 13819–13840 (2012).
35. Yang, G., Pan, F. & Gan, W.B. Stably maintained dendritic spines are associated with lifelong memories. *Nature* **462**, 920–924 (2009).
36. Albrecht, J. *et al.* Extracellular concentrations of taurine, glutamate, and aspartate in the cerebral cortex of rats at the asymptomatic stage of thioacetamide-induced hepatic failure: modulation by ketamine anesthesia. *Neurochem. Res.* **25**, 1497–1502 (2000).
37. Forde, B.G. & Lea, P.J. Glutamate in plants: metabolism, regulation, and signalling. *J. Exp. Bot.* **58**, 2339–2358 (2007).
38. Sano, C. History of glutamate production. *Am. J. Clin. Nutr.* **90**, 728S–732S (2009).
39. Nguyen, Q.T. *et al.* An *in vivo* biosensor for neurotransmitter release and *in situ* receptor activity. *Nat. Neurosci.* **13**, 127–132 (2010).
40. Singer, J.H. & Diamond, J.S. Vesicle depletion and synaptic depression at a mammalian ribbon synapse. *J. Neurophysiol.* **95**, 3191–3198 (2006).
41. Moussawi, K., Riegel, A., Nair, S. & Kalivas, P.W. Extracellular glutamate: functional compartments operate in different concentration ranges. *Front. Syst. Neurosci.* **5**, 94 (2011).

ONLINE METHODS

Animal husbandry. All experiments were conducted according to protocols approved by the Institutional Animal Care and Use and Institutional Biosafety Committees of the Howard Hughes Medical Institute, Janelia Farm Research Campus, or of the relevant institutions where the work was performed.

Construct availability. pCMV.iGluSnFR (41732) and pRSET.GltI253-cpGFP.L1LV/L2NP (41733) have been deposited at Addgene. AAV.hSynapsin.iGluSnFR (PV2723) and AAV.GFAP.iGluSnFR (PV2722), along with the Cre recombinase-dependent versions AAV.hSynapsin.FLEX-iGluSnFR (PV2724) and AAV.CAG.FLEX-iGluSnFR (PV2725), are available from the University of Pennsylvania Vector Core (<http://www.med.upenn.edu/gtp/vectorcore/>).

Sensor engineering and characterization. Methods for generating constructs and linker variants are essentially the same as described previously¹⁸. Briefly, the gene for *E. coli* glutamate-binding protein (*gltI*) was subcloned from a previous glutamate sensor, FLIP-E¹⁶ into the pRSET-A vector (Invitrogen) with a BamHI site encoding glycine-serine at the 5' end and an EcoRI site included after the stop codon. The *GltI*-cpGFP insertion variants were constructed by overlap PCR using the wild-type *gltI* sequence and the cpGFP146 variant from a previously described maltose sensor¹⁸. Linker variants were generated by site-directed mutagenesis and screened in a high-throughput manner as described previously¹⁸. Detailed amino acid sequences are provided in **Supplementary Figures 2 and 5–7**.

Protein expression and purification. Plasmids containing the *GltI*-cpGFP variants were transformed into *E. coli* BL21(DE3) cells (lacking pLysS). Protein expression was induced by growth in liquid auto-induction medium supplemented with 100 µg/ml ampicillin at 30 °C (ref. 42). Proteins were purified by immobilized Ni-NTA affinity chromatography⁴³ in 0.1 M sodium phosphate buffer containing 1 M NaCl, pH 7.4. The *GltI*-cpGFP proteins were eluted with a 120-mL gradient from 0 mM to 200 mM imidazole.

Glutamate titrations. Ligand-binding data were fit to a single-binding site isotherm, as before¹⁸.

Membrane-anchored iGluSnFR (HEK293 cells). For mammalian expression, the *GltI253-cpGFP.L1LV/L2NP* gene was cloned into the pDisplay vector (Invitrogen) between the BglII and PstI sites. A variant of pDisplay lacking the hemagglutinin tag, which we termed pCMV(MinDis), was generated by PCR assembly. HEK293 cells were transiently transfected with pCMV(MinDis).GltI253-cpGFP.L1LV/L2NP, also referred to as pCMV.iGluSnFR, and grown in high-glucose DMEM supplemented with 10% FBS and 2 mM glutamine. After 2 d incubation at 37 °C in 35-mm microwell dishes on no. 1.5 coverslips, cells were extensively, but gently, rinsed with Hank's balanced salt solution (Gibco) and imaged with a modified Olympus BX microscope controlled with ScanImage software v.3.6 (<http://www.scanimage.org/>) and an Olympus 60×/0.9-NA LUMPlanFI/IR objective. Two-photon fluorescence excitation was evoked with a laser (Chameleon Vision II; Coherent Inc.) tuned to 910 nm. Fluorescence emission was passed through a 565-nm dichroic mirror and BG22 emission

filter and measured using a photomultiplier tube (Hamamatsu). Images were acquired at a resolution of 512 × 512 pixels at two frames per second. For glutamate titration experiments, images were obtained at 10-s intervals for 2 min at each concentration. The steady-state fluorescence level at each concentration was calculated from images acquired in the second minute only.

Neuronal culture characterization. A mixed cell culture (neurons and glia) was prepared from Sprague-Dawley rat pups (Charles River Laboratories). Briefly, P0 pups were decapitated, and the brains were dissected into ice-cold neural dissection solution (NDS, 10 mM HEPES (Sigma) in HBSS (Invitrogen), pH 7.4). Hippocampi were removed, enzymatically digested with papain (~60 units), washed with pre-warmed plating medium (PM) and then mechanically digested by trituration. Cells were plated on coverslips coated with Matrigel matrix (BD Biosciences), and kept at 37 °C, 5% CO₂ in PM for ~24 h and then in growth medium (GM) for the duration with medium exchanges every 4 d. After 3 d, they were infected with AAV.hSynapsin.iGluSnFR or AAV.GFAP.iGluSnFR and grown for 2 weeks before characterization. Infected neurons were stimulated using a custom-built field stimulator with platinum wires and imaged using either an Olympus IX81 motorized, inverted microscope (10×/0.4-NA objective, Chroma ET-GFP or ET-TxRed filter sets) equipped with an EMCCD camera (Andor iXon+ 897, 34.8 frames per second) or a confocal fluorescence scope 510 (20× or 60× objective). Field stimuli were delivered at 40-V, 30-Hz, 1-ms pulses for the following trains: 1, 2, 3, 5, 10, 20, 40, 80 and 160 field stimuli. Buffer exchange for glutamate titrations was performed with a laminar flow chamber from C&L Instruments. The images were analyzed using MATLAB (MathWorks).

Glutamate uncaging in acute hippocampal slice. AAV2/1.hSynapsin.iGluSnFR alone or AAV2/1.hSynapsin.FLEX-iGluSnFR combined with AAV2/1.Cre at various dilutions was bilaterally injected into the hippocampus of P23–P29 male Sprague-Dawley rats. 10–35 d later, acute transverse hippocampal slices were prepared as previously described⁴⁴, according to methods approved by the Janelia Farm Institutional Animal Care and Use and Institutional Biosafety Committees. Briefly, animals were deeply anesthetized with isoflurane and transcardially perfused with ice-cold cutting solution containing (in mM): 220 sucrose, 28 NaHCO₃, 2.5 KCl, 1.25 NaH₂PO₄, 0.5 CaCl₂, 7 MgCl₂, 7 glucose, 3 Na-pyruvate and 1 ascorbic acid, saturated with 95% O₂ and 5% CO₂. The brain was quickly removed and sectioned in cutting solution with a Vibratome (Leica). Slices were incubated in a submerged holding chamber in ACSF at 37 °C for 45 min and then stored in the same chamber at room temperature. For recording, slices were transferred to the submerged recording chamber of the microscope where experiments were performed at 34–37 °C in ACSF containing (in mM): 125 NaCl, 3 KCl, 25 NaHCO₃, 1.25 NaH₂PO₄, 1.3 CaCl₂, 1 MgCl₂, 25 glucose, 3 Na-pyruvate and 1 ascorbic acid, saturated with 95% O₂ and 5% CO₂. Hippocampal pyramidal neurons were visualized using an Olympus BX-61 epifluorescence microscope equipped with infrared Dodt optics and a water immersion lens (60×/0.9 NA, Olympus). Current-clamp whole-cell recordings from the somata of hippocampal pyramidal neurons were performed with a Dagan BVC-700 amplifier in active 'bridge' mode, filtered at 3 kHz and digitized at 50 kHz. Patch pipettes (3–6 M) were filled with a solution containing

(in mM): 134 K-gluconate, 6 KCl, 10 HEPES, 4 NaCl, 4 Mg₂ATP, 0.3 Tris₂GTP, 14 Na-phosphocreatine and 0.05 Alexa 594 (Invitrogen), pH 7.25. Series resistance, monitored throughout the experiment, was <20 M. All neurons had resting membrane potentials between −61 and −68 mV (−65.0 ± 0.5 mV, mean ± s.e.m., *n* = 6). Steady-state apparent input resistance was 67.0 ± 6.1 MΩ. Rheobase was 233 ± 21 pA. All parameters are within the normal ranges of hippocampal pyramidal neurons⁴⁵. A dual galvanometer-based two-photon laser scanning system (Prairie Technologies) was used to image neurons and to focally uncage glutamate at individual dendritic spines. Two ultrafast pulsed laser beams (Chameleon Ultra II; Coherent) were used: one at 880 and 920 nm for imaging Alexa 594 and iGluSnFR, respectively, and one at 720 nm to photolyze MNI-caged L-glutamate (Tocris; 10 mM, dissolved in freshly carbogenated ACSF, applied via pressure ejection through a pipette above the slice). Laser beam intensity was independently controlled with electro-optical modulators (model 350-50, Conoptics). Uncaging dwell time was 0.2 ms. Line-scan imaging through spines was performed at 600–1,200 Hz with dwell times of 8–12 μs for <400 ms. Particular care was taken to limit photodamage as well as bleaching of iGluSnFR during imaging and uncaging. This included limited low-power scanning of dendrites and spines of interest as well as the use of a passive 8× pulse splitter in the uncaging path in most experiments to drastically reduce photodamage⁴⁶. Basal fluorescence of both channels was continuously monitored as an indicator of damage to cellular structures and/or bleaching of fluorophores. Multiple trials (3–12) were performed at each imaging location for each uncaging intensity level with a duty cycle of >10 s. Individual traces (EPSPs and iGluSnFR line-scan profiles) from the same paradigm were averaged with no smoothing, filtering or background subtraction for analysis and presentation using custom-written macros in IgorPro and MATLAB.

Mouse retinal imaging *in vitro*. Retinas were prepared using standard methods⁴⁷. Briefly, adult (1.5–6 months) Black6 (C57BL/6J) mice (Charles River Laboratories) of either sex were injected intravitreally with AAV as follows. First, a mouse was anesthetized with isoflurane (3%) and placed under a dissection microscope. Ventilation with isoflurane (1.5%) was continued for the duration of the procedure (5–10 min). A drop of the topical analgesic proparacaine (0.5%; Bausch & Lomb) was applied to each eye, followed by a drop of tropicamide (0.5%; Bausch & Lomb) to dilate the pupil and paralyze the ciliary muscle. We injected 0.8–1.0 μl of AAV2/1.hSynap.iGluSnFR in H₂O (2.0 × 10¹² IU/μl) into the vitreous humor of the eye using a custom-designed syringe (Borghuis Instruments). After 14–21 d, eyes were removed and dissected in oxygenated Ames medium (95% O₂–5% CO₂; Sigma-Aldrich). The retina was removed from the sclera and placed on an upright Olympus BX-51 microscope. Retinas were perfused with oxygenated Ames medium at physiological temperature (34–36 °C) throughout the recordings. Two-photon fluorescence measurements were made with ScanImage software v.3.6 (<http://www.scanimage.org/>)⁴⁸ using an Olympus 60×/0.9-NA, LUMPlanFI/IR objective and an ultrafast pulsed laser (Chameleon Vision II; Coherent) tuned to 910 nm. Images (512 × 128 pixels) were acquired at 16 frames per second; line scans were obtained at 2 kHz and downsampled to 500 Hz for presentation in **Figure 4** (box-car average). In some experiments, visual stimuli were generated with a miniature DLP projector

(Pico, Texas Instruments) focused on the photoreceptors through the condenser lens of the microscope. Image size on the retina was 580 × 800 μm; pixel size was 1.2 × 1.2 μm. A dichroic filter limited stimulus wavelengths to 420–460 nm; irradiance was 0.1–1 mW/cm². For experiments in which imaging was combined with electrophysiological recording and pharmacological manipulations, we used a Dell video projector (M109s DLP) modified to project UV light⁴⁹ with a single LED (NC4U134A, peak wavelength 385 nm; Nichia). Filtering by the projector's optics shifted the peak of the stimulus light to 398 nm. A 440-nm short-pass dichroic filter (Semrock) prevented stimulus light from reaching the photon multiplier tubes. Image size on the retina was 2.1 × 2.8 mm; irradiance was 0.1 mW/cm². Data were analyzed with custom algorithms in MATLAB. Modulated responses to drifting gratings were quantified by Fourier analysis.

Patch electrodes (5–8 MΩ) were filled with the following intracellular solution (in mM): 120 Cs-methanesulfonate, 5 TEA-Cl, 10 HEPES, 10 BAPTA, 3 NaCl, 2 QX-314-Cl, 4 ATP-Mg, 0.4 GTP-Na₂ and 10 phosphocreatine (pH 7.3, 280 mOsm). Excitatory currents were recorded near the chloride reversal potential *E*_{Cl} (−67 mV) after correcting for the liquid junction potential (−9 mV).

Imaging *in vivo* in *C. elegans*. In the nerve ring, the promoter *rig-3* (neuronal IgCAM-3) drives strong expression solely in the AVA neurons and provides a reliable genetic entry point into the cell. Injection of *rig-3::iGluSnFR* and *rig-3::RCaMP1e* produced worms expressing both sensors in AVA. Imaging was performed on F₁ progeny of CX14651 *kyEx4786* [*rig-3::RCaMP1e*, *unc-122::GFP*] and CX14652 *kyEx4787* [*rig-3::iGluSnFR*, *unc-122::dsRed*] animals, or F₁ progeny of CX14653 *eat-4(ky5); kyEx4786* and CX14654 *eat-4(ky5); kyEx4787* animals. Young adult hermaphrodites, bearing both transgenes, at approximately 14–20 h after the L4 larval stage, were trapped in a PDMS microfluidic device as previously described⁵⁰ and illuminated with a HB100 Hg lamp (Zeiss) mounted on an Axiovert 100TV inverted microscope (Zeiss). Dual excitation of iGluSnFR and RCaMP1e was performed using a Chroma 51022x dichroic excitation filter followed by a Chroma 51022bs dichroic beam splitter. The fluorescence light path was split and projected onto two halves of an Andor iXon camera using a Dual-View beam splitter (Optical Insights) with a 565-nm long-pass filter. Chroma S510/30 and S650/75 emission filters were used for the short- and long-wavelength beam paths, respectively. A 200 μm × 100 μm field of view was imaged at 100 f.p.s. with a 40× Apochrome oil objective (Zeiss), and MetaMorph software was used to acquire movies. Fluorescence from the neuronal process and cell body was quantified using in-house scripts for the MetaMorph software (Molecular Devices). The resulting fluorescence traces were background corrected and normalized to maximum fluorescence so that the dynamic range of measurements ranged from 0 to 1 for each indicator and each trace.

A leaky integrator model, implemented in MATLAB, was used to fit the normalized RCaMP signal (the 'output') from the normalized iGluSnFR signal (the 'input')

$$\text{Modeled_Calcium}(t) = e^{(-dt/\tau)} \times \text{Modeled_Calcium}(t-1) + \text{Expt_Glutamate}(t)$$

where Modeled_Calcium (0) is defined as 0.0, *dt* is the sampling time (0.1 s) and *τ* is a leak constant, varied from 0 to 20 s.

Minimizing the r.m.s. error (RMSE) between Modeled_Calcium (t) and Expt_Calcium (t)—both normalized to run between 0 and 1—was used to select the value of τ that best fit a given trial. The τ values for the eight trials were then averaged, and the resulting best-fit τ was used to re-fit the eight trials.

In vivo imaging of visually evoked glutamate transients in the tectal neuropil of zebrafish larvae. *mitfa*^{-/-} (nacre) or *mitfa*^{-/-}, *roy*^{-/-} (casper) zebrafish^{51,52} (obtained from the Zebrafish International Resource Center) were maintained under standard conditions (in a circulating water system (ZebTEC, Tecniplast) at 28 °C and a 14:10 h light:dark cycle⁵³. Larvae were raised in E3 embryo medium containing (mM) 5 NaCl, 0.17 KCl, 0.33 CaCl₂ and 0.33 MgSO₄. Embryos were injected at the 1- to 4-cell stage with 12 ng/ μ l plasmid DNA encoding Gal4FF⁵⁴ under the control the pan-neuronal *elavl3/HuC* promoter (*elavl3:Gal4FF*), 8 ng/ μ l plasmid DNA encoding *iGluSnFR* or *GCaMP5G* downstream of four nonrepeating upstream activation sequences (4Xnr UAS) designed to minimize silencing by CpG methylation⁵⁵ and 40 ng/ μ l *Tol2* transposase mRNA diluted in E3 medium with 0.025% phenol red. *Tol2* sequences flanking the expression cassettes allowed for stable genomic integration.

At 6 d post-fertilization (d.p.f.), larvae (which have as yet undetermined sex at this age) were mounted as in previous studies³⁴ (using low melting point agarose, Invitrogen) and imaged on a custom-built two-photon microscope with a mode-locked Ti:sapphire laser system (Spectra-Physics) tuned to 920 nm and a water-immersion objective (XLUMPlanFLN 20 \times /1.0 W; Olympus). A 36 μ m \times 36 μ m square region of the optic tectum neuropil, containing the dendrites of labeled tectal neurons, was selected for imaging. Although cell bodies of neurons in the periventricular region were also well labeled, we did not observe fluorescence changes in these areas. Images were acquired at 22.47 Hz (*iGluSnFR*) or 5.85 Hz (*GCaMP5G*) using software custom-written in LabVIEW (National Instruments).

Visual stimuli were generated with Microsoft DirectX and projected onto a flat opal glass screen underneath the larvae using the red channel of a MicroVision PicoP laser projector. An additional long-pass filter (590 nm) was placed in front of the projector to prevent bleed-through into the fluorescence collection pathway. For stimulation, a black bar of 1 mm thickness was displayed for 8 s at the edge of a red 4.2 \times 4.2-cm square centered on the fish before drifting across the screen at 2 cm/s. The bar was swept in the four cardinal directions, and each direction was presented three times.

To visualize local fluorescence changes during visual stimulation, the imaging area was tiled evenly with 2.0 μ m \times 2.0 μ m square regions of interest spaced at 2.0- μ m intervals. The background light level (detected while the laser was attenuated by a Pockels cell during scanning) was subtracted from each trace. Baseline fluorescence (F) was defined as the median fluorescence in the period before the onset of visual motion, and each trace was converted to units of $\Delta F/F$. To generate the average response trace for comparison of kinetics, each trace was first aligned in time to be maximally correlated with the average. For the latency maps, response time was defined as the point of maximal fluorescence.

In vivo glutamate imaging of layer V apical dendrites in mouse motor cortex. Six ICR outbred mice (female), purchased from the Jackson Laboratory and group housed in the NYU

Berg Central Animal Facility, were injected at P15 with AAV2/*1.hSynapsin.iGluSnFR* in primary motor cortex 2 weeks before imaging experiments (0.2–0.3 μ l at a titer of 2×10^{13} genomic copies per milliliter). At P30, mice were prepped for awake animal surgery. A head holder composed of two parallel micro-metal bars was attached to the animal's skull to reduce motion-induced artifacts during imaging and motor training. First, surgical anesthesia was achieved with an intraperitoneal injection (5–6 μ l/g) of a mixture of ketamine (20 mg/ml) and xylazine (3 mg/ml). A midline incision of the scalp exposed the periosteum, which was manually removed with a microsurgical blade. A small skull region (~0.2 mm in diameter) was located over the left motor cortex on the basis of stereotactic coordinates (1.0 mm lateral from the midline at bregma; forelimb region)^{35,56} and marked with a pencil. A thin layer of cyanoacrylate-based glue was first applied to the top of the entire skull surface and to the metal bars, and the head holder was then further fortified with dental acrylic cement (Lang Dental Manufacturing). The dental cement was applied so that a well was formed, leaving the motor cortex with the marked skull region exposed between the two bars. All procedures were performed under a dissection microscope. After the dental cement was completely dry, the head holder was screwed to two metal cubes that were attached to a solid metal base, and a cranial window was created over the previously marked region. The procedures for preparing a thinned-skull cranial window for two-photon imaging have been described in detail in previous publications⁵⁷. Briefly, a high-speed drill was used to carefully reduce the skull thickness by approximately 50% under a dissecting microscope. The skull was immersed in ACSF during drilling. Skull thinning was completed by carefully scraping the cranial surface with a microsurgical blade to ~20 μ m in thickness. For awake animal imaging, the completed cranial window was covered with silicon elastomer (World Precision Instruments), and mice were given at least 4 h to recover from the surgery-related anesthesia. Upon awakening, mice with head mounts were habituated for a few times (10 min each time) in the treadmill-adapted imaging apparatus to minimize potential stress effects of head restraining, motor training and imaging. Awake animals were head restrained in the imaging apparatus, which sits on top of a custom-built free-floating treadmill. Here, the silicon elastomer was peeled off to expose the thinned skull region and replaced by ACSF.

These *in vivo* two-photon imaging experiments were performed using an Olympus Fluoview 1000 two-photon system (tuned to 910 nm) equipped with a Spectra Physics MaiTai DeepSee. The average laser power on the sample was ~20 mW. All experiments were performed using a 25 \times objective immersed in an ACSF solution and with a 3 \times –4 \times digital zoom. Most images were acquired at frame rates of 10 Hz (2- μ s pixel dwell time). Image acquisition was performed using FV10-ASW v.2.0 software and analyzed *post hoc* using ImageJ software (NIH). $\Delta F/F$ was calculated identically to *in vitro* imaging experiments. For detection of glutamate signals at dendritic spines, a line crossing the dendrite and the middle of the spine head was drawn.

42. Studier, F.W. Protein production by auto-induction in high density shaking cultures. *Protein Expr. Purif.* **41**, 207–234 (2005).

43. Crowe, J. et al. 6xHis-Ni-NTA chromatography as a superior technique in recombinant protein expression/purification. *Methods Mol. Biol.* **31**, 371–387 (1994).



44. Harnett, M.T., Makara, J.K., Spruston, N., Kath, W.L. & Magee, J.C. Synaptic amplification by dendritic spines enhances input cooperativity. *Nature* **491**, 599–602 (2012).
45. Magee, J.C. Dendritic hyperpolarization-activated currents modify the integrative properties of hippocampal CA1 pyramidal neurons. *J. Neurosci.* **18**, 7613–7624 (1998).
46. Ji, N., Magee, J.C. & Betzig, E. High-speed, low-photodamage nonlinear imaging using passive pulse splitters. *Nat. Methods* **5**, 197–202 (2008).
47. Borghuis, B.G. *et al.* Imaging light responses of targeted neuron populations in the rodent retina. *J. Neurosci.* **31**, 2855–2867 (2011).
48. Polgruto, T.A., Sabatini, B.L. & Svoboda, K. ScanImage: flexible software for operating laser scanning microscopes. *Biomed. Eng. Online* **2**, 13 (2003).
49. Wang, Y.V., Weick, M. & Demb, J.B. Spectral and temporal sensitivity of cone-mediated responses in mouse retinal ganglion cells. *J. Neurosci.* **31**, 7670–7681 (2011).
50. Chalasani, S.H. *et al.* Dissecting a circuit for olfactory behaviour in *Caenorhabditis elegans*. *Nature* **450**, 63–70 (2007).
51. Lister, J.A., Robertson, C.P., Lepage, T., Johnson, S.L. & Raible, D.W. *nacre* encodes a zebrafish microphthalmia-related protein that regulates neural-crest-derived pigment cell fate. *Development* **126**, 3757–3767 (1999).
52. White, R.M. *et al.* Transparent adult zebrafish as a tool for *in vivo* transplantation analysis. *Cell Stem Cell* **2**, 183–189 (2008).
53. Westerfield, M. *The Zebrafish Book* 2nd edn. (University of Oregon Press, Eugene, Oregon, USA, 1994).
54. Asakawa, K. & Kawakami, K. Targeted gene expression by the Gal4-UAS system in zebrafish. *Dev. Growth Differ.* **50**, 391–399 (2008).
55. Akitake, C.M., Macurak, M., Halpern, M.E. & Goll, M.G. Transgenerational analysis of transcriptional silencing in zebrafish. *Dev. Biol.* **352**, 191–201 (2011).
56. Tennant, K.A. *et al.* The organization of the forelimb representation of the C57BL/6 mouse motor cortex as defined by intracortical microstimulation and cytoarchitecture. *Cereb. Cortex* **21**, 865–876 (2011).
57. Yang, G., Pan, F., Parkhurst, C.N., Grutzendler, J. & Gan, W.B. Thinned-skull cranial window technique for long-term imaging of the cortex in live mice. *Nat. Protoc.* **5**, 201–208 (2010).